Effect of nanoparticle size on the near-surface pH-distribution in aqueous and carbonate buffered solutions

Thomas Stepan [a,*], Lisa Tété [b], Lila Laundry-Mottiar [c], Elena Romanovskaia [d,e], Yolanda S. Hedberg [c,d,f], Herbert Danninger [a], Michael Auinger [a,g,g,a,*]

[a] *Institute of Chemical Technologies and Analytics, Technische Universität Wien, Getreidemarkt 9, 1040 Vienna, Austria*
[b] *Department of Chemistry, Umeå University, SE-90187 Umeå, Sweden*
[c] *Department of Chemistry, University of Western Ontario, London, Ontario, N6A 5B7, Canada*
[d] *Div. Surface and Corrosion Science, Department of Chemistry, KTH Royal Institute of Technology, SE-10044 Stockholm, Sweden*
[e] *Department of Materials Science and Engineering, University of Virginia, Charlottesville, VA, 22904, USA*
[f] *Surface Science Western, The University of Western Ontario, London, Ontario, N6G 0J3, Canada*
[g] *WMG, University of Warwick, Coventry CV4 7AL, United Kingdom*

ABSTRACT

An analytical solution for the effect of particle size on the current density and near-surface ion distribution around spherical nanoparticles is presented in this work. With the long-term aim to support predictions on corrosion reactions in the human body, the spherical diffusion equation was solved for a set of differential equations and algebraic relations for pure unbuffered and carbonate buffered solutions. It was shown that current densities increase significantly with a decrease in particle size, suggesting this will lead to an increased dissolution rate. Near-surface ion distributions show the formation of a steep pH-gradient near the nanoparticle surface (<6 μm) which is further enhanced in the presence of a carbonate buffer (<2 μm). Results suggest that nanoparticles in pure electrolytes not only dissolve faster than bigger particles but that local pH-gradients may influence interactions with the biological environment, which should be considered in future studies.

1. Introduction

Nanoparticles (i.e. particles in the nanometre size range) have gained an immense interest during the past decades. The high surface-to-volume ratio of these particles has led to applications in the area of heterogeneous catalysis [1], especially for electrochemical reactions involving the oxygen reduction/evolution reaction (ORR/OER) and CO_2 reduction [2–4], to enhance mechanical properties of alloys [5,6] and for biomedical applications [7] such as nanosheets and nanozymes for catalytic use [8,9]. Due to their small size, nanoparticles can easily be absorbed by the human body and engulfed by cells (endocytosis) through a variety of exposure routes, such as inhalation, ingestion, injection, and dermal exposure [10–13]. This uptake mechanism can be used to deliver drugs and for different biomedical applications, including the di-

agnosis and treatment of different diseases [14–17]. The relatively high uptake and surface reactivity of nanoparticles, as compared to microparticles [18,19] can, however, cause adverse health effects [20]. This is best demonstrated by the fact that air pollution with fine particulate matter (<2.5 μm), primarily caused by combustion processes, is one of the leading threats to global public health [21]. Increasing dissolution with decreasing size (from 50 to 5 nm) has also been demonstrated for relatively inert gold nanoparticles in specific environments [22,23]. Different physicochemical properties of the particles are important for toxic outcomes and pharmacokinetic behaviour and fate, including size, size distribution, aggregation, shape, surface charge, solubility, crystallinity, and surface groups including protein/polymer corona [24,25]. Apart from these factors influencing the toxicity and biocompatibility of such particles, local pH-shifts, caused by chemical reactions, will severely affect the local environment around these particles, which has implications on the dissolution rate and electrocatalytic activity. In a previous study [26], it was shown that small currents can lead to significant shifts of the pH-value near a planar electrode surface. Due to the high kinetic rates of the hydrogen oxidation reaction

---

* Corresponding author(s) at: Institute of Chemical Technologies and Analytics, Technische Universität Wien, Getreidemarkt 9, 1040 Vienna, Austria.
E-mail addresses: thomas.stepan@gmx.at (T. Stepan), michael.auinger@tuwien.ac.at (M. Auinger).
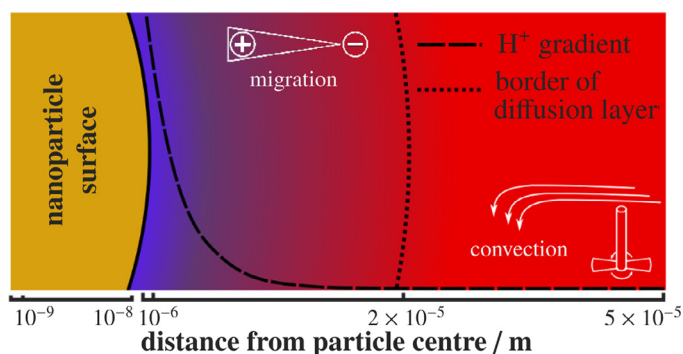
Fig. 1. Graphical illustration of the relative sizes in the general modelling concept for the ion distribution near the solid-liquid interface. The mechanisms of the main transport phenomena - diffusion, migration and convection are highlighted. The difference of the electrochemical potential, termed *surface potential* in this study, between the particle surface (solid line) and the end of the diffusion zone (dotted line) leads to a gradient of the H$^+$ distribution (dashed line) across the diffusion zone surrounding the nanoparticle. Please note the different scaling of the *x*-axis.

Table 1
Pre-factors and diffusion coefficients used for the calculations.

species	pre-factor	D at 25 °C (m^2 s^{-1})	Literature
H$^+$	+1	9.31×10^{-9}	[29]
OH$^-$	-1	5.27×10^{-9}	[29]
H$_2$CO$_3$	+2	2.04×10^{-9}	[30]
HCO$_3^-$	0	1.10×10^{-9}	[30]
CO$_3^{2-}$	-2	0.80×10^{-9}	[30]

(HOR) and the hydrogen evolution reaction (HER), the equilibrium between H$_2$, H$_2$ and OH$^-$ at the solid-liquid interface is important, but still often misinterpreted, or its contribution to the overall current signal is ignored. This is because electrolytes often have a very low concentration of dissolved H$_2$ which quickly leads to diffusion limitation of the anodic current signal (HOR, acidic surface pH). The majority of nanotoxicity-related research focuses on body fluids, which contain a rather complex mix of amino acids, salts and other substances. Due to the complex composition and the lack of thermodynamic data, it is hard to model the system in its full complexity. Hence, this work reports on a simplified approach to simulate the local pH-distribution from an analytic function of surface potential and particle size in unbuffered and carbonate buffered solution, providing useful insights to understand *1*) the pH-shifts in close proximity to the nanoparticle surface and *2*) size effects of the nanoparticles on the near-surface ion distribution. Because analytical solutions compute much faster than numerical simulations, they are more useful for parametric studies of such electrolyte systems.

2. Fundamental concept

The local concentration of a chemical species *i* can change by transport effects such as diffusion, migration, convection or by involvement in a chemical reaction that consumes or produces this species. In aqueous solutions, the reactions between ions such as H$^+$ and OH$^-$ are extremely fast, much faster than ion transport via diffusion, migration and convection [27]. Therefore, the concentration of OH$^-$ can be expressed by the concentration of H$^+$ and the equilibrium coefficient of the reaction between both ions. This means that the chemical reaction between ionic species can be assumed to be in local thermodynamic equilibrium, and the general modelling approach contains the relationships for element transport and the algebraic relations between chemical species via thermodynamic equilibrium considerations [26]. The influence of transport phenomena such as diffusion, migration and convection on the ion distribution is shown in Fig. 1.

2.1. Model development

A general solution for the time-dependent problem mentioned above cannot be derived and hence reasonable simplifications to the general case need to be made. Some of these simplifications have already been discussed for flat electrode surfaces [26] and are briefly described in Appendix A. We assume that the shape

of the nanoparticles is spherical, which allows a transformation of the relevant equations into spherical coordinates. Due to the high symmetry of a sphere, only the radial terms need to be considered for Eq. (1). Whilst this may lead to deviations for experiments on partially covered or embedded particles, reasonable comparison of obtained results with free (radial) ion transport can still be drawn. Nanoparticles with an ellipsoid shape do not have a simple analytical expression for their surface and the transformation of the main transport equation into an ellipsoidal coordinate system does not lead to an explicit analytical solution either [28]. However, the ion distributions along the three main axes can still be approximated by individual numerical simulations. Alternatively, the analytical solutions for the three curvatures of the ellipsoid can be calculated via Eq. (1), before these are averaged to provide an approximation of the macroscopic behaviour in experiments with an electrode with (spherical) nanoparticles.

$$\frac{\partial c_i}{\partial t} = \frac{1}{r^2} div\left(r^2 D_i \nabla c_i + r^2 \frac{D_i z_i e_0}{k_B T} c_i \nabla \phi \right) \qquad (1)$$

c_i.......concentration of species i in mol m^{-3}
t.......time in s
D_i.......diffusion coefficient of species i in m^2 s^{-1}
z_i.......charge of species i
ϕ.......(electrochemical) surface potential vs. standard hydrogen electrode (SHE) in V
T.......absolute temperature in K
k_B.......Boltzmann constant ($k_B = 1.380 \times 10^{-23}$ J K^{-1})
e_0.......elementary charge ($e_0 = 1.602 \times 10^{-19}$ A s)
r.......radius (distance from particle) in m

All calculations in this work are based on a diffusion layer thickness that would form in a rotated disk electrode setup at a rotation rate of 2500 rounds per minute (rpm) and a kinematic viscosity of 0.9×10^{-7} m^2 s^{-1}, which is the value for pure water at 25 °C [29]. The diffusion coefficients are listed in Table 1.

Given that reaction rates of the HOR/HER on most metallic surfaces are extremely high [1] and reactions between ions are fast [27], the system can be considered to be in local thermodynamic equilibrium at any time. Thus, the pH at the particle surface corresponds to the surface potential of H$^+$/H$_2$ via the Nernst equation.

$$E = E^0_{H^+/H_2} + \frac{RT}{2F} ln\left(\frac{a^2_{H^+}}{a_{H_2}} \right) = -59 \; mV \; pH - 28.5 \; mV \; log_{10}(p_{H_2}) \quad (2)$$

E.......(electrochemical) surface potential at the particle surface in V vs. standard hydrogen electrode (SHE)
a_i.......activity of species i (hydrogen, protons)
pH.......pH-value at the particle surface
R.......universal gas constant ($R = 8.3144$ J mol^{-1} K^{-1})
F.......Faraday constant ($F = 96485$ A s mol^{-1})
p_{H_2}.......partial pressure of H$_2$

2.2. Analytical solution for the steady state

Due to the fast transport and kinetics of the solution reactions such as the water equilibrium and the (de-)protonation of carbonic acid [27,29], the cyclic voltammograms and the local ion concentrations, including the pH-value, reach a steady state after a few

microseconds. Consequently, the time derivative $\partial c_i / \partial t$ in the simulations can be set to zero. After setting the migration term to zero for electrolytes with high ionic strength (see Appendix A) and integrating Eq. (1) with respect to the axis perpendicular to the particle surface, one obtains Fick's first law of diffusion in spherical coordinates. Finally, after multiplying the diffusive flux j with the Faraday constant F and integration, the current density can be calculated as follows:

$$k^* - \frac{j}{r} = -F \sum_i (n_i - m_i) D_i c_i \qquad (3)$$

where j is the current density in A m^{-2}, r is the radial distance from the particle surface in m, k^* is the integration constant, n_i is the pre-factor for proton capture and m_i is the pre-factor for proton supply. A list of pre-factors for all relevant species in this study can be found in Table 1. Inserting the boundary conditions for the concentration of H$^+$ at the particle surface ($r = r_0$) and the outer boundary of the diffusion layer at ($r = r_0 + \delta_{\text{eff}}$), respectively, determines the current density j for a given surface pH-value. The solution of this polynomial function provides the local distribution of the representative species across the diffusion zone. The distribution of the other participating species can then be derived from their thermochemical equilibrium conditions, which will be discussed in Section 3. Since the local distribution of all species involved is connected by the local pH-value, it is reasonable to select H$^+$ as the representative species throughout this study.

2.3. Numerical solution for diffusion limitation

The limited supply of hydrogen and oxygen via diffusion to the surface is considered in the calculations for surface potentials above 0 V$_{\text{SHE}}$ to compare with typical experimental conditions. Depletion of dissolved hydrogen near the electrode surface becomes significant at potentials above -100 mV$_{\text{SHE}}$. Therefore, the flux of hydrogen, required to sustain the local pH-value, is calculated from a mass and charge balance for all hydrogen transporting species (H$^+$, OH$^-$, H$_2$CO$_3$, HCO$_3^-$, CO$_3^{2-}$ and H$_2$), which leads to Eq. (4). Since experiments were performed without a controlled hydrogen partial pressure in the atmosphere, we assumed $p_0 = 1$ mbar H$_2$ to be in equilibrium for the calculations. Considering this, one obtains the hydrogen partial pressure at the electrode surface, according to Eq. (4). This value is then added to the Nernst equation (Eq. (2)) to derive the corresponding surface potential.

$$p_{\text{H}_2} = p_0 + \frac{1}{6 D_{\text{H}_2} H_{\text{H}_2}} \left[D_{\text{H}_+} \left(c_{\text{H}_+}^{\text{surface}} - c_{\text{H}_+}^{\text{solution}} \right) - D_{\text{OH}_-} K_W \left(\frac{1}{c_{\text{H}_+}^{\text{surface}}} - \frac{1}{c_{\text{H}_+}^{\text{solution}}} \right) \right.$$
$$\left. + 4 D_{\text{H}_2\text{CO}_3} \left(c_{\text{H}_2\text{CO}_3}^{\text{surface}} - c_{\text{H}_2\text{CO}_3}^{\text{solution}} \right) + D_{\text{HCO}_3^-} \left(c_{\text{HCO}_3^-}^{\text{surface}} - c_{\text{HCO}_3^-}^{\text{solution}} \right) - 2 D_{\text{CO}_3^{2-}} \left(c_{\text{CO}_3^{2-}}^{\text{surface}} - c_{\text{CO}_3^{2-}}^{\text{solution}} \right) \right]$$
$$(4)$$

where H_{H_2} is the Henry constant for the solubility of hydrogen at 25 °C.

The oxygen diffusion limitation can be observed at potentials more negative than -600 mV$_{\text{SHE}}$ and has been considered by restricting the negative current densities in the simulations to typical values, reported in literature ($j = 0.014$ mA mm^{-2}, [31]). A small parallel ohmic resistance was included in the calculations to compensate for the tilt in experimental RDE results, described in Appendix B.

3. Results and discussion

The obtained modelling approach has already been verified for the case of planar surfaces in unbuffered solutions as well as acetate, borate and phosphate buffered solutions at potentials below the diffusion limitation in previous works [26]. Therefore, this section focuses on the effect of the particle size, which influences the

curvature of the surface. For an infinite particle radius ($r_0 \to \infty$), the surface is mathematically flat and hence results converge to the values for flat electrodes. By solving the general mathematical relationship for a given diffusion zone thickness in both unbuffered and carbonate buffered solutions, one obtains results in the form of a cyclic voltammogram. By solving the corresponding polynomial for the distance (Eq. (3)), the local ion distribution and changes of the pH-value will be shown. Results are representative for single nanoparticles. It should be noted that agglomerations and/or a high density of nanoparticles might lead to an overlap of the diffusion profiles. This will in turn lead to a change of the macroscopic effect, as described in more detail in numerical simulations in [32,33].

3.1. Unbuffered solution

For the case of an unbuffered solution, only H$^+$ and OH$^-$ contribute to the current transport. Following the principles outlined in Section 2.2. and substituting the concentration of OH$^-$ by the thermodynamic equilibrium with H$^+$ (Eq. (5)), one obtains Eq. (6), expressing the relationship for the total current density as a function of surface pH-value. The local pH-distribution can then be derived from the solutions of the corresponding polynomial equation, leading to the analytical expression shown in Eq. (7).

$$K_W = c_{\text{H}_+} \, c_{\text{OH}_-} = 10^{-14} mol^2 \, L^{-2} \qquad (5)$$

$$j_{\text{H}_+/\text{OH}_-} = \frac{1}{\frac{1}{r_0} - \frac{1}{\delta_{\text{eff}} + r_0}} \left[D_{\text{H}_+} \left(c_{\text{H}_+}^{\text{surface}} - c_{\text{H}_+}^{\text{solution}} \right) - D_{\text{OH}_-} K_W \left(\frac{1}{c_{\text{H}_+}^{\text{surface}}} - \frac{1}{c_{\text{H}_+}^{\text{solution}}} \right) \right] \qquad (6)$$

$$c_{\text{H}_+ (r)} = -\frac{k^* - \frac{j}{r}}{2 F D_{\text{H}_+}} \pm \sqrt{\frac{\left(k^* - \frac{j}{r} \right)^2}{4 F^2 D_{\text{H}_+}^2} - \frac{D_{\text{OH}_-}}{D_{\text{H}_+} K_W}} \qquad (7)$$

Figure 2 shows the calculated cyclic voltammograms for different particle sizes at a given solution pH-value of 7. A second x-axis at the top of the figure shows the surface pH-value, derived from the corresponding surface potential (Eq. (2)). A closer look at Eq. (6) reveals that the calculated current density j depends on the particle radius r_0. Considering that the diffusion equation is solved for one nanoparticle, it stands to reason that larger particles exhibit a larger current signal. Thus, in order to compare different sizes of nanoparticles with each other, the current signal has to be normalized. It is often a matter of controversy and ease of measurement whether this normalization should be respective to the total mass of the particle or respective to the surface area. In order to circumvent this discussion and because both versions are easily accessible from modelling, it was decided to plot both normalized currents in Fig. 2. This furthermore allows the reader to compare between surface-specific and mass-specific current densities. It should be noted that due to the small mass and surface area of these nanoparticles, the corresponding normalized current densities appear to be very high. In an experiment, where nanoparticles would be embedded in, or attached to, a conductive matrix, the exposed nanoparticle surface area is small. Hence experimentally observed current densities would in fact be much lower and below the diffusion limiting current in an environment saturated with 1 bar H$_2$ at 25 °C [1,34].

According to the CV curves in Fig. 2a, the current density features a plateau region at neutral surface pH, independent of particle size. This plateau does not correspond to a kinetic hindrance of the reaction, but rather to a significant change of the surface pH. In near-neutral solution (pH 6-8), the concentrations of H$^+$ and OH$^-$ are very small and hence only a minimal current is required to significantly alter the pH-value near the particle surface. However, whereas the plateau is limited to a potential range of -500 mV$_{\text{SHE}}$
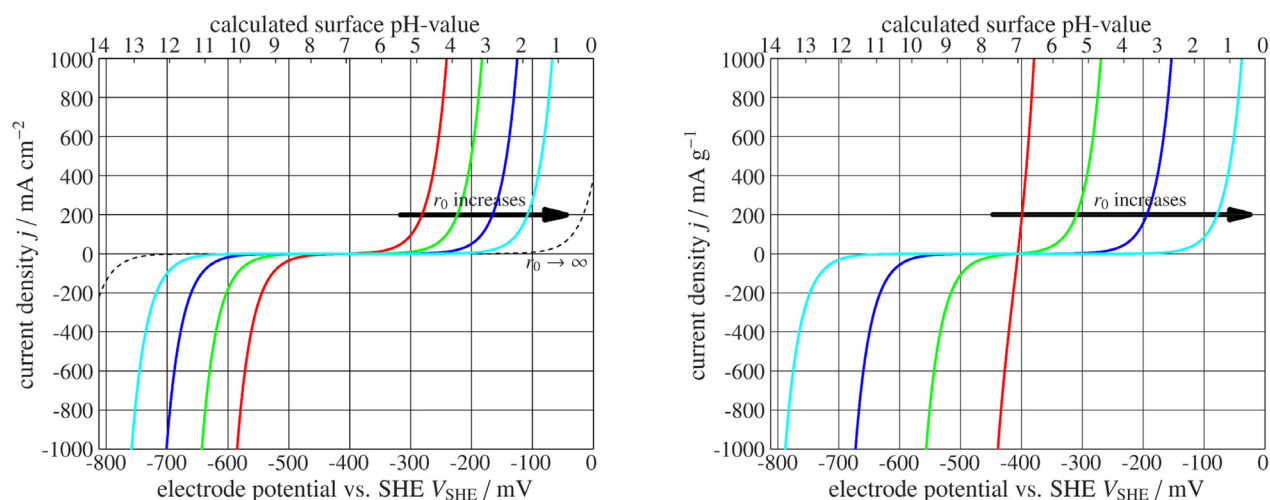
Fig. 2. Calculated cyclic voltammograms for a range of different nanoparticle sizes (1 nm, 10 nm, 100 nm, 1000 nm) in unbuffered aqueous solutions of pH 7. The current densities in the graphs are normalized to the particle surface area (left) and particle mass (right), respectively. The black line in the left figure represents the current density for a planar surface, meaning an infinitely large particle radius ($r_o \to \infty$).
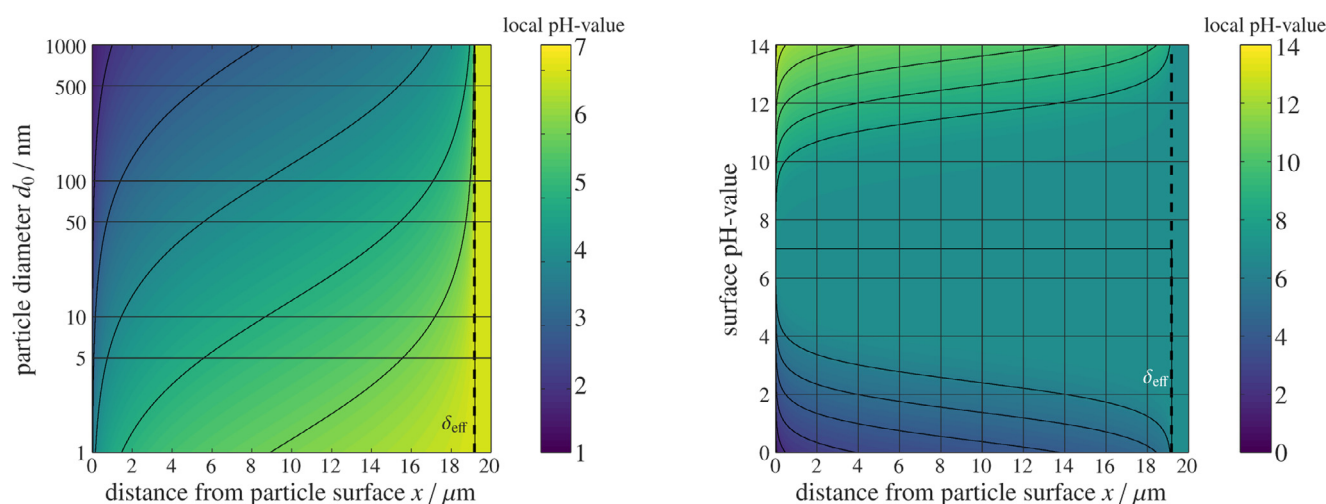
Fig. 3. Contour plots for the radial pH-distribution across the diffusion zone in unbuffered solution with pH 7. Impact of particle diameter at a surface pH-value of 1.5 (similar to gastric liquid, left) and impact of surface pH-value for a 10 nm sized nanoparticle (right).

to -400 mV$_{SHE}$ for a particle diameter of 1 nm, it significantly extends for larger particles up to a range from -650 mV$_{SHE}$ to -200 mV$_{SHE}$ ($\approx$pH 11-3) for a particle diameter of 1000 nm. This observation indicates that smaller particles feature steeper concentration gradients across the diffusion zone, leading to higher current density values. Larger particles on the other hand, characterized by a decreasing curvature of the surface, feature smoother concentration gradients and behave increasingly similar to planar surfaces as indicated by the black dashed curve in Fig. 2a. Whereas the particle surface area scales with r^2, normalization to the particle weight leads to an even higher scaling factor (r^3). Consequently, Fig. 2b shows a significantly larger impact of particle size on the calculated current density. For a complementary discussion regarding the influence of the solution pH-value and other parameters such as electrode rotation rate on the current signal, the reader is referred to previous investigations [26]. The local pH-value distribution near the particle surface can be calculated using Eq. (7). Results for a range of nanoparticle sizes from 1 nm up to 1000 nm with surface pH 1.5 (similar to gastric fluid, -87 mV$_{SHE}$) and in neutral solution (pH 7, -406 mV$_{SHE}$) are shown in Fig. 3a. Figure 3b illustrates the change of pH-value for a constant nanoparticle size under varying surface pH-values / surface potential. In ac-

cordance with the set boundary conditions, the local pH outside the diffusion zone ($x \geqslant \delta_{eff}$) is only dependent on the bulk solution pH-value. By contrast, the pH-distribution inside the diffusion layer is governed both by solution and surface pH-values as well as the particle diameter. According to Fig. 3a, the pH-gradient gets increasingly steeper with smaller particle diameter and shifts towards the particle surface. Very small particles ($<$10 nm) feature a steep pH-gradient up to approximately 9 μm distance from their surface. Whilst this diffusion layer thickness is almost 1000 times larger than the size of these particles themselves, these steep gradients lead to the high current densities shown in Fig. 2. The chosen surface pH of 1.5 defines a most extreme acidic environment inside this small volume around the particles, as it can be found in gastric liquid [35,36], caused by inflammatory conditions and macrophages [37], or strongly oxidizing conditions such as Fenton reactants, hydrogen peroxide or hypochlorous acid [37,38]. However, the outer layer of the diffusion zone is characterized by moderate pH-value changes. Larger particles ($>$100 nm) on the other hand, exhibit a smoother pH-distribution across the entire diffusion zone, thus leading to systematically lower specific current densities than smaller particles. The contour plot in Fig. 3b exemplifies the impact of a variation of the surface pH value in neutral
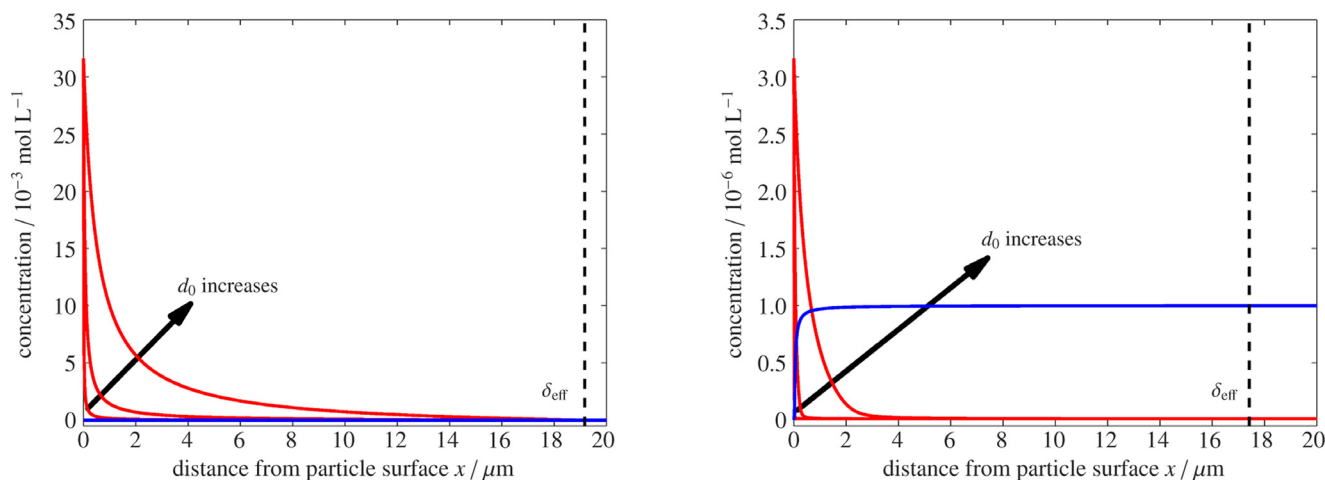
Fig. 4. Ion distribution of H$^+$ (red lines) across the diffusion zone for 10 nm, 100 nm and 1000 nm sizes nanoparticles. The OH$^-$ concentration (blue line) is shown for a nanoparticle diameter d_0 of 10 nm for comparison. a) solution pH 7, surface pH 1.5 (similar to gastric fluid); b) solution pH 8.8 (similar to bile and pancreatic fluid), surface pH 5.5 (normal skin pH).

solution. As a consequence of the pH 7 solution, the contour lines are symmetrical around this pH-value. For moderate surface pH values (pH 5-9), only minimal deviations between diffusion zone and bulk solution can be observed. Changes are mostly limited to the direct vicinity of the particle surface and are indistinguishable on the linear distance scale. Larger differences occur, however, if highly acidic or alkaline surface pH-values are chosen. Whilst for particles of 10 nm in size, these regions with extreme pH-values are limited to a comparably small fraction of the diffusion zone, they can grow significantly in size for even smaller particles.

Figure 4 shows the ion distribution of H$^+$ and OH$^-$ at any point in the diffusion zone for various particle sizes as a function of solution pH-value. Due to the low surface pH-value, the current signal in the diffusion zone corresponds mainly to hydronium diffusion as shown in Fig. 4a, which changes if the bulk solution becomes alkaline (see Fig. 4b). In this case, the contribution of OH$^-$ dominates the overall current signal, with the exception of the acidic particle surface, where the concentration of H$^+$ rises accordingly. As mentioned previously, increasing the particle size results in a flatter and overall smoother concentration gradient across the diffusion zone. Whereas the H$^+$-distribution of 1000 nm particles extend far into the diffusion zone, a 10 nm particle features a very steep H$^+$-gradient directly at the particle surface. The steepness of the concentration gradient also depends on the pH-value difference between the solution and the nanoparticle surface. A comparison between Fig. 4a (bulk pH 7) and Fig. 4b (bulk pH 8.8) reveals that alkaline solutions results in steeper concentration gradients and may therefore lead to higher currents if the ionic concentrations are similar.

3.2. Carbonate buffer system

The carbonate-bicarbonate buffer equilibrium is critical for maintaining a near neutral pH-value ($\approx$pH 7.4) in our blood stream [39,40]. The concentration of the three involved buffer species H$_2$CO$_3$, HCO$_3^-$ and CO$_3^{2-}$ are related to the proton concentration according to the following equilibria:

$$H_2CO_3 \rightleftharpoons HCO_3^- + H^+ \rightleftharpoons CO_3^{2-} + 2H^+ \tag{8}$$
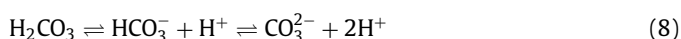
Carbonic acid is able to provide 2 H$^+$, whereas the carbonate anion is able to capture 2 protons. The net contribution of bicarbonate to the reaction is zero, since HCO$_3^-$ may function as donor or acceptor of one proton. Therefore, the corresponding pre-factors in Eq. (A.2) and Table 1 are +2 for carbonic acid, 0 for the bicarbon-

ate anion and -2 for the carbonate anion. Therefore, the calculation of the current density for the carbonate buffered system is slightly more complex, since two additional terms for the (de-)protonation reactions, as shown in Eqs. (9) & (10), have to be considered

$$K_{a1} = \frac{c_{H^+} c_{HCO_3^-}}{c_{H_2CO_3}} = 10^{-6.35} \; mol \; L^{-1} \tag{9}$$

$$K_{a2} = \frac{c_{H^+} c_{CO_3^{2-}}}{c_{HCO_3^-}} = 10^{-10.33} \; mol \; L^{-1} \tag{10}$$

Furthermore, the concentration of the buffer species can be substituted by one constant value (c_{buffer}^0), equalling the total buffer concentration in Eq. (11)

$$c_{buffer}^0 = c_{H_2CO_3} + c_{HCO_3^-} + c_{CO_3^{2-}} \tag{11}$$

Inserting these relationships into the general form for the current density in Eq. (3), one obtains Eq. (12). Similar to the unbuffered case, the solution of the polynomial for the distance gives the local pH-values across the diffusion zone, shown in Eq. (13). Due to the high degree of the polynomial, an analytical form for these solutions cannot be given and instead this equation was solved algebraically as described in [26].

$$j = j_{H^+/OH^-} + \frac{c_{buffer}^0 F}{\frac{1}{r_0} - \frac{1}{r_0 + \delta_{eff}}} \left(\frac{2D_{H_2CO_3} c_{r,H^+}^2 - 2D_{CO_3^{2-}} K_{a1} K_{a2}}{c_{r,H^+}^2 + K_{a1} c_{r,H^+} + K_{a1} K_{a2}} \right) \tag{12}$$

$$D_{H^+} c_{H^+}^4 + \left(D_{H^+} K_{a1} + 2D_{H_2CO_3} c_{buffer}^0 + \frac{k^* - j/r}{F} \right) c_{H^+}^3 + \left(\frac{k^* - j/r}{F} K_{a1} + D_{H^+} K_{a1} K_{a2} - D_{OH^-} K_W \right) c_{H^+}^2$$
$$+ \left(\frac{k^* - j/r}{F} K_{a1} K_{a2} - D_{OH^-} K_{a1} K_W - 2D_{CO_3^{2-}} c_{buffer}^0 K_{a1} K_{a2} \right) c_{H^+} - D_{OH^-} K_{a1} K_{a2} K_W = 0 \tag{13}$$

It should be noted that the analytical expression for the current density in Eq. (12) can be expressed by the contributions of H$^+$ and OH$^-$. It is hence corresponding to the current density in an unbuffered solution j_{H^+/OH^-} and an additional term for the buffer species. Figure 5 shows the calculated cyclic voltammetry curves for the surface-area-specific current densities of 10 nm sized nanoparticles in the presence of different concentrations of carbonate buffer at a solution pH of 7.4, which is similar to the pH-value in human blood. Independent of the buffer concentration, the current is zero when the surface pH-value equals the pH-value of the solution. In this case, all concentration gradients across the diffusion zone are zero, consequently no diffusive flux occurs. In contrast to the unbuffered solution (red curve), the curves of the buffered solutions exhibit a split of the characteristic plateau domain across the pK$_a$-values of the carbonate buffered system. In
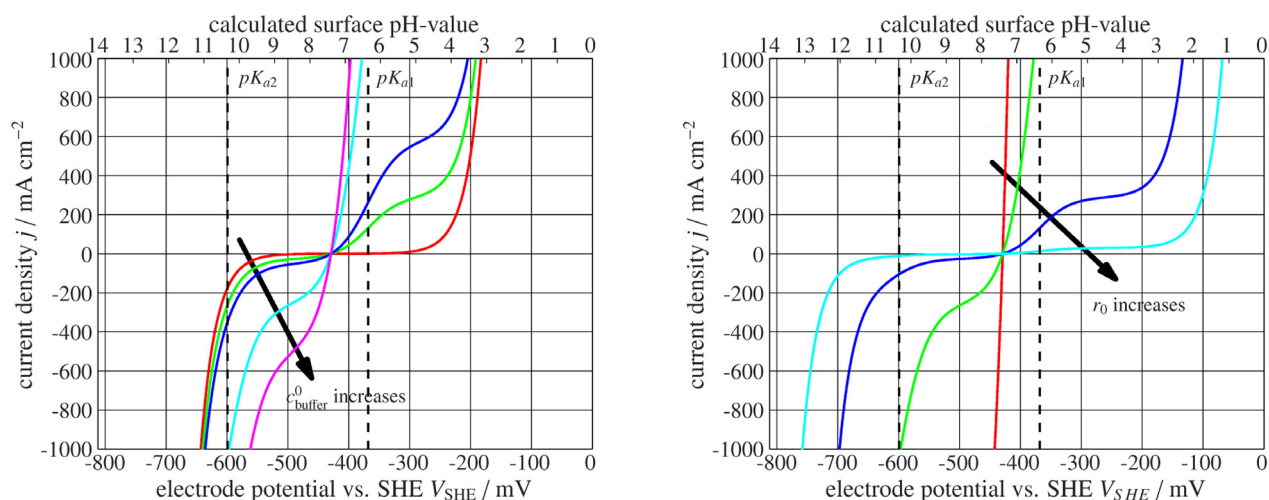
Fig. 5. Cyclic voltammograms of nanoparticles in unbuffered and carbonate buffered systems at pH 7.4, similar to human blood. All current densities have been normalized to the particle surface area. a) impact of buffer concentration (unbuffered solution, 0.5 mM, 1 mM, 5 mM and 10 mM carbonate buffer) for a 10 nm sized nanoparticle; b) impact of particle diameter (1 nm, 10 nm, 100 nm and 1000 nm) on current signal in 5 mM carbonate buffered solution.

general, the additional buffer species cause an increase of the current signal, related to the surface pH-value and the buffer concentration, leading to the formation of these steps in the CV-curves. Since bicarbonate is neutral with regard to its capacity as a proton carrier, the smallest effects are observed in the neutral pH-domain, in between the two pK_a-values (6.35, 10.33) of the carbonate system. For moderately acidic surfaces (pH 4-6), the contribution of H_2CO_3 dominates the diffusive flux, most readily observed by the significant deviations of the curves in this pH-range. The contribution of the buffer species scales linearly with the total buffer concentration, which can also be concluded from Eq. (12). At extreme surface pH-values, the concentration of H^+ or OH^-, respectively, exceeds the comparably small amount of bicarbonate buffer by far, hence the current signal is dominated by the contribution of the unbuffered solution (j_{H^+/OH^-}). Figure 5b compares the current signal for various particle diameters at a set buffer concentration of 5 mM. When comparing the different curves, it is obvious that the calculated current density increases with decreasing particle diameter. This is conceivable, considering that the additional term for the carbonate species in Eq. (12) is subject to the same particle-size dependent pre-factor as the term for the unbuffered solution. As a consequence, the actual impact of the addition of 5 mM carbonate buffer on the calculated current density is specific to the particle size. Thus, according to Fig. 5b, the general statement regarding the particle size effect in unbuffered solutions still holds true for carbonate buffered solutions.

Similar to the unbuffered solution, the local proton concentration across the diffusion zone for carbonate buffered solutions can be obtained by solving the polynomial in Eq. (13). The contour plots in Fig. 6 illustrate the local pH-distribution at every point in the diffusion zone. Similar to the contour plots for the local pH-value in unbuffered media, Fig. 6a exemplifies the impact of varying the particle diameter for a solution of pH 7.4 and a particle surface pH 1.5, whereas Fig. 6b depicts the pH-distribution for a constant particle diameter of 10 nm as a function of the surface pH-value. Compared to the unbuffered solution, the addition of only 1 mM carbonate buffer already shows a distinct impact on the pH-distribution across the diffusion layer, as the obvious role of a buffer is to keep the pH-value constant. In particular for small particles ($d_0 < 10$ nm), the neutral pH-domain extends far into the diffusion layer up to 3 µm distance from the particle surface. For larger particles, the buffer effect is less pronounced, although still ascertainable. Fig. 6b offers a different point of view, focusing on

the variation of the surface pH-value. As opposed to the unbuffered solution, the bicarbonate buffer is able to neutralize both H^+ as well as OH^- ions, stabilizing the neutral pH-domain across a wider range of surface pH-values. The buffer capacity scales primarily with the total concentration of buffer ions (c_{buffer}^0) in the solution, although the solution pH plays an important role as well. Due to its pK_a-values at 6.35 and 10.33, the carbonate system is ideal to buffer near neutral solutions.

The ion distribution of H^+ and OH^- in unbuffered, as well as 1 mM and 10 mM carbonate buffered solutions, is shown in Fig. 7a. All curves were calculated by setting the particle diameter to 10 nm and using a solution and surface pH-value of 7.4 and 1.5, respectively. Based on the H^+-distribution presented in Fig. 7a, it can be concluded that carbonate buffered solutions feature an increasingly steeper H^+-gradient, scaling with the total buffer concentration. In addition, the contribution of the buffer species to the current transport leads to a change of the concentration gradients across the diffusion zone and is the primary cause for the increasing current densities of carbonate buffered solutions, observed in Fig. 5a. The ion distribution of the buffer species is depicted in Fig. 7b. Since the stability of the buffer species is governed by the local pH-value, carbonic acid is the dominant ion species near the acidic particle surface. Reflecting the increasing pH-value, the concentration of H_2CO_3 drops in the direction of the bulk solution, whereas the concentration of the bicarbonate ion increases. This indicates that the proton transport near the acidic particle surface is dominated by H^+, whereas the buffer species take over this role at approximately 1.5 µm distance from the surface. Bearing in mind that bicarbonate is inert regarding its role as proton shuttle (Table 1), the impact of the carbonate buffer in this case can be primarily attributed to the contribution of carbonic acid. Due to the overall low concentration, the third buffer species CO_3^{2-} plays only a minor role in the investigated pH-range (1.5–7.4) but becomes dominant in strongly alkaline media. Outside the diffusion zone ($x > \delta_{eff}$), the solution pH is constant, hence, the concentration of the buffer species remains constant as well.

3.3. Experimental verification for flat surfaces using a rotating disk electrode

Experimental measurements, using a glassy carbon rotating disk electrode (i.e. flat surface $r_0 \to \infty$, setup described in Appendix B), showed an overall good agreement with simulations (see Fig. 8)
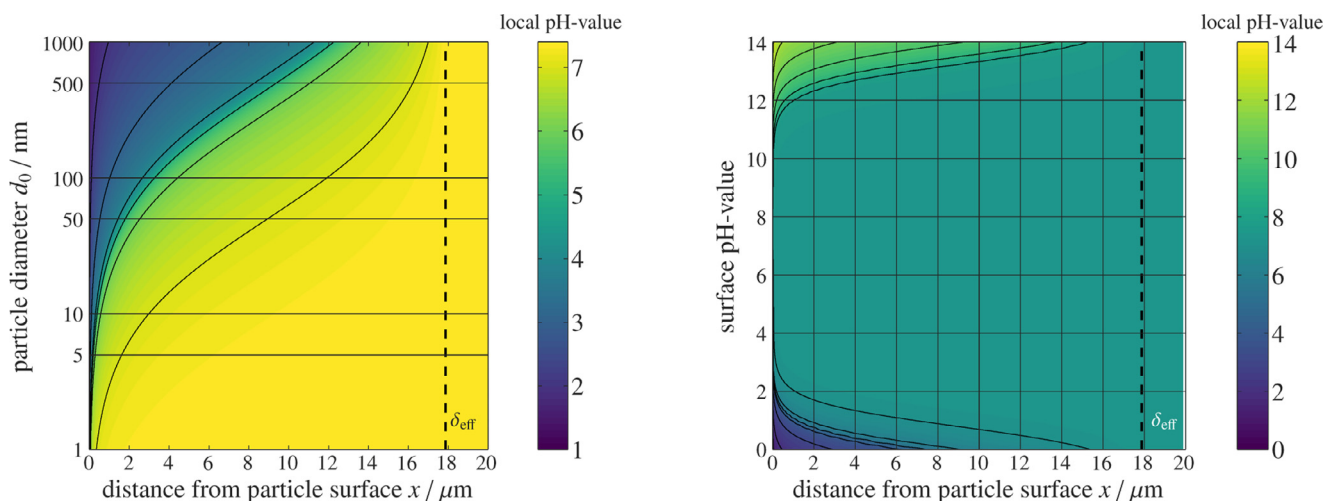
Fig. 6. Contour plots for the radial pH-distribution across the diffusion zone in 1 mM carbonate buffered solution with pH 7.4, similar to human blood. Impact of particle diameter at a surface pH-value of 1.5 (similar to gastric fluid, left) and impact of surface pH-value for a 10 nm sized nanoparticle (right).
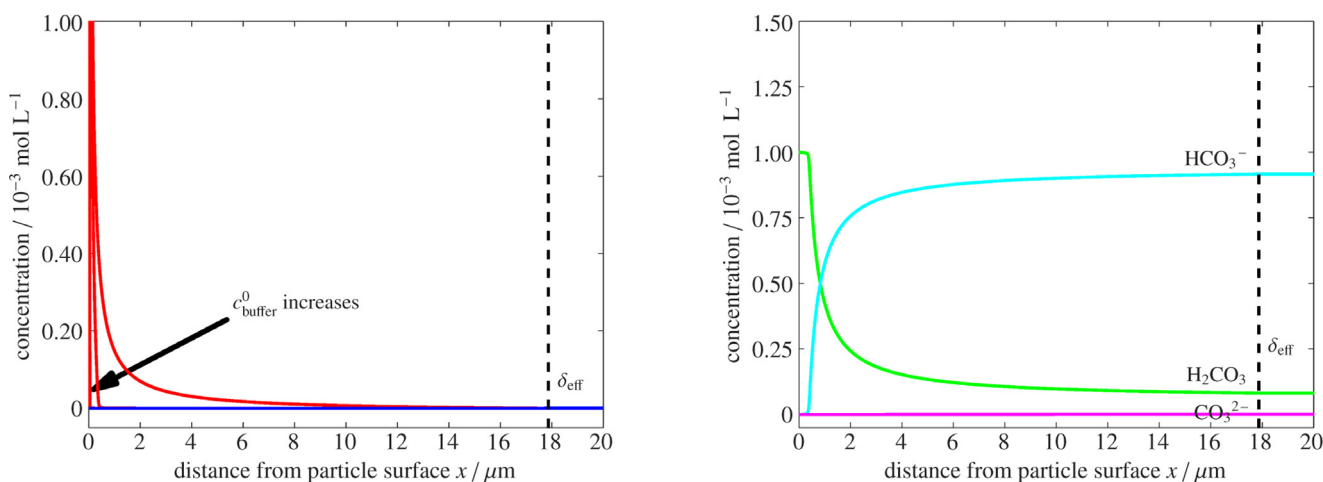
Fig. 7. Ion distributions across the diffusion zone of a nanoparticle with diameter $d_0 = 10$ nm in solution with pH 7.4 (similar to human blood) and pH 1.5 at the surface (similar to gastric fluid). Left: Concentration of H^+ (red lines) for unbuffered solution, 1 mM and 10 mM carbonate buffered solutions. The OH^- concentration (blue line) for the unbuffered solution is shown for comparison. Right: Local concentrations of buffer species H_2CO_3, HCO_3^- and CO_3^{2-} in 1 mM carbonate buffered solution.
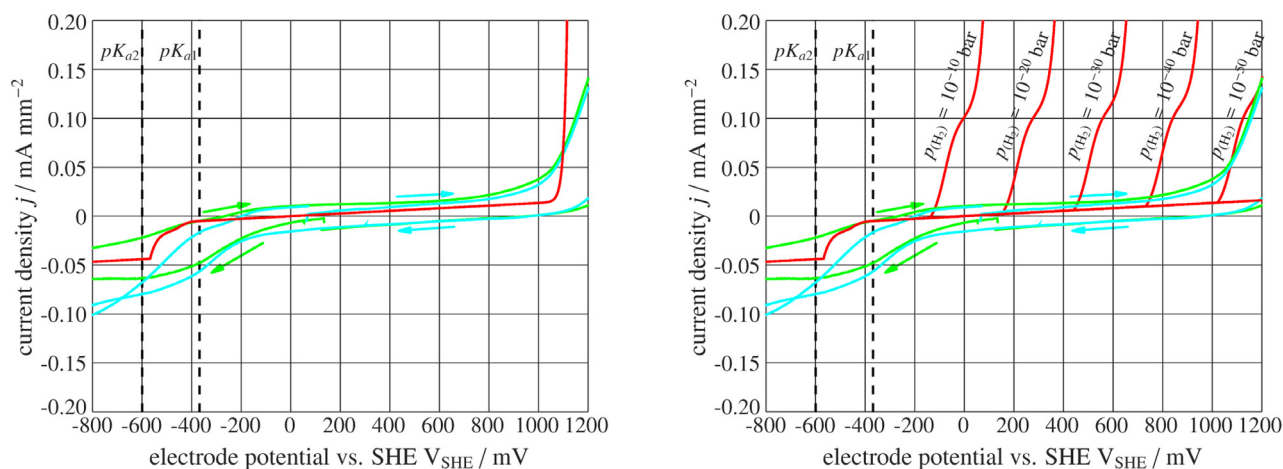
Fig. 8. Comparison between experimental (green and cyan lines) and modelled (red lines) cyclic voltammetry curves of a rotating disk electrode setup at pH 7.4 and 22 °C with a 5 mM carbonate buffer in 5 g NaCl L^{-1}. The scan direction in the experiments is indicated by the arrows. The simulations in the left image include the Butler-Volmer kinetics of the oxygen evolution reaction (OER) and allow the hydrogen partial pressure at the surface to drop to zero. The right image excludes the current contribution for the OER and shows the influence of a lower limit for the hydrogen activity at the electrode surface on the calculated current signal for a 1 mM carbonate buffer. A small parallel ohmic resistance of 75 Ω was added to all simulated values to compensate for the tilt of experimental current densities.

when the simulations have been extended by diffusion limitation of the chemical species. In all measurements, a small hysteresis could be observed (different currents for forward and backward scans). Plateau values for the current density near the pK_a values of the buffer become visible. The depletion of hydrogen near the surface can be seen at potentials more positive than -100 mV$_{SHE}$, thus changing the surface potential and forming a large plateau in the range between -100 mV$_{SHE}$ and 700 mV$_{SHE}$.

The experimental current densities show a steep increase near 800 mV$_{SHE}$, which is in theoretical agreement with the onset of the oxygen evolution reaction (OER) [41] because the calculated surface pH-value remains at ≈ 7.4 between -400 mV$_{SHE}$ and 1300 mV$_{SHE}$. However, the fitted exchange current density ($j_0 = 14$ mA mm^{-2}) for this reaction would be higher than typical values reported in literature [42]. Whilst the onset potential does not match the oxidation of carbon ($E^0_{C/CO_2} = 0.207$ V, $E^0_{C/CO} = 0.518$ V [43]) it should also be noted that the transition of the current signal is not purely exponential, giving rise to the assumption that the hydrogen partial pressure at the surface may not drop to zero but instead remains constant at approximately 10^{-50} bar H$_2$ ($\Delta G^0_r = 200$ kJ mol^{-1} at pH 7.4). Such small values are indicative for an equilibrium partial pressure when hydrogen and carbon are interacting via a weak chemical bond (compare $\Delta G^0_r = 335$ kJ mol^{-1} for the average value of a covalent C-H bond). This would indicate that the surface of the glassy carbon electrode may be (partially) terminated with hydrogen. Whilst an experimental proof of this hypothesis remains to be explored in detail, it should be noted that the observed non-ideality can nevertheless be fitted by the shift of the carbonate buffer signal with the hydrogen partial pressure equilibrium at the surface.

3.4. Importance of main findings

Combining the results from previous sections, one can see that the current density increases for smaller nanoparticles as it is also experimentally observed for gold [44] and silver [45]. This leads to steeper pH-gradients in close proximity to the nanoparticle surface which in turn will increase the dissolution rate. A significant change of pH-value may even alter the tertiary/quaternary structure of large proteins and amino acids, hence affecting the binding between biomolecules and nanoparticles. Simulations have shown that the current transport across the diffusion zone is not always carried out by the same ions. Especially in the presence of a carbonate buffer, the buffer ions will dominate the ion transport under near-neutral pH-values. This has implications on the local solubility of metal ions and may lead to the formation of precipitates. If these precipitates form close to the surface, as one would expect for small nanoparticles, they might act as a barrier and hamper further dissolution. For larger particles, precipitates will form at a larger distance from the surface and hence get washed away more easily. Dissolution of nanoparticles will change the particle radius with time and hence lead to an increase of the local ion gradients and current density. Whilst a transient behaviour was not modelled in this work, one can easily estimate from the relationship $t \propto \delta^2_{eff}/D$ that the timeframe for diffusion in close proximity to the nanoparticle surface has to be in the range of milliseconds. This appears to be faster than typical dissolution rates and the ion distributions in equilibrium, shown in Figs. 3, 4, 6 and 7 can thus be considered as the ion distributions for a given nanoparticle size in an experimental setup. The simulations in this study focussed on the geometric effects of spherical nanoparticles on the near-surface ion distribution which is influenced by nanoparticle size. Elliptic shapes were not calculated since the complexity of the equations requires numerical simulations and does not allow for an explicit analytical solution [28] of the local ion distributions. Effects of agglomeration and inhomogeneous distributions will ad-

ditionally alter the macroscopic effect, as it is also reported from numerical simulations in literature [32,33]. Thermodynamic properties and their change with nanoparticle size, as described in [46], were not considered and it is expected that including these would further increase the dissolution rate for smaller nanoparticles.

4. Conclusions

An analytical solution for the calculation of cyclic voltammetry curves and local pH-values near the surface of spherical nanoparticles in (un-)buffered solutions has been presented. Results are discussed for the specific case of a carbonate buffer and agglomerate-free nanoparticle suspensions. The spherical geometry leads to a change of the local ion distributions, which become steeper for smaller particles, thus resulting in higher current densities. For large nanoparticles (up to 1 μm), the ion gradients are overall smoother and increasingly similar to the results for planar surfaces. Whilst the simulation results are calculated for a single nanoparticle, the current density has been normalized, with respect to the nanoparticle surface and nanoparticle mass, in order to relate to quantities, which can be easier accessed experimentally. The addition of a carbonate buffer extends the region of the near neutral pH-value, resulting in steeper ion gradients and higher current densities. Again, this effect is most pronounced for small nanoparticles and would indicate a higher dissolution rate for smaller nanoparticles. It should, however, be noted that, depending on particle composition, the formation of carbonate precipitates might occur which in turn will affect the dissolution rate. Especially for biological applications, it should also be noted that significant changes of the pH-value near the surface will have an effect on the protonation state of amino acids. Experimental results for flat surfaces ($r_0 \rightarrow \infty$) using a rotating disk electrode set-up and simulations including diffusion limitation of hydrogen and oxygen are in good agreement despite the complexity of the electrolyte. The depletion of hydrogen near the surface leads to the formation of an extended plateau area at surface potentials more positive than -100 mV vs. standard hydrogen electrode. Whilst an increase of the current density above 800 mV$_{SHE}$ could be observed in the experiments due to the oxygen evolution reaction (OER), simulations were also able to replicate the current signal if the lower limit for the hydrogen partial pressure at the surface was kept constant at a value near 10^{-50} bar H$_2$. Whilst an experimental proof for this mathematical fit was not the aim of this study, it should be noted that the derived binding energy may indicate an interaction of remaining hydrogen and the carbon surface.

Declaration of Competing Interest

The authors declare that they have no known competing financial interests or personal relationships that could have appeared to influence the work reported in this paper.

Credit authorship contribution statement

Thomas Stepan: Methodology, Software, Writing – original draft. **Lisa Tété:** Methodology, Software, Writing – review & editing. **Lila Laundry-Mottiar:** Investigation, Validation, Writing – review & editing. **Elena Romanovskaia:** Investigation, Validation, Writing – review & editing. **Yolanda S. Hedberg:** Conceptualization, Supervision, Writing – review & editing. **Herbert Danninger:** Supervision, Project administration, Writing – review & editing. **Michael Auinger:** Conceptualization, Supervision, Software, Writing – review & editing.

Acknowledgements

Appendix A. Simplification of the modelling approach

An adequate treatment of transport by convection around nanoparticles via the incompressible Navier-Stokes equation is very complex. Assuming a laminar flow around a spherical particle, the thickness of the diffusion layer, formed around the sphere, will not be uniform. In fact, uniform flow patterns would only be obtained if the particle itself would be acting as source or as sink for the flow, which is physically impossible. Hence, different points near the particle surface experience different flow velocities, resulting in varying diffusion layer thicknesses. Considering this as well as the shear-dependence of viscosity makes the determination of a precise flow pattern unreasonable. Hence, a simplified approach was chosen as a good average for the inhomogeneous flow around such particles where only the effects of diffusion and migration remain. *Migration*, meaning the movement of ions due to a gradient of surface potential (electric field), is very low in biological fluids, owing to the high concentration of salts [39,40], which results in a high ionic strength of the electrolyte. Therefore, the contribution of migration to the overall movement of a species i should be negligible in the mathematical model [1,34]. For experimental verification of the model in previous studies, the migration term in Eq. (1) can be suppressed by increasing the total ionic strength of the solution by adding an inert electrolyte such as NaCl or NaClO$_4$. Considering all these conditions, only *diffusion*, the transport of elements by a gradient of the concentration, will remain from the mathematical terms in the general modelling approach. The diffusion layer thickness is dependent on the viscosity of the solution, the flow conditions, and the diffusion coefficient of the species. It was mentioned that a uniform flow pattern was chosen due to the high number of uncertainties in the non-Newtonian flow behaviour. This leads to a modelled constant thickness of the diffusion zone around spherical shaped nanoparticles. Therefore, the 3-dimensional spherical geometry can be simplified to the radial term of the partial differential equation. From a modelling point of view, the diffusion layer thickness is a scaling factor, and therefore preserves the unique shape of the current signal and the pH-value distribution in the diffusion zone. This still allows for general conclusions to be drawn from this work. Furthermore, this approach enables the derivation of an analytical expression, as opposed to a series of numerical computations. Also, comparison of a similar modelling approaches for flat surfaces with experimental data obtained by a commonly used rotary disk electrode (RDE) setup has been reported [26]. Following this idea, the thickness of the diffusion layer in this study can be approximated by the Koutecky-Levich equation [34] (Eq. (A.1)):

$$\delta_i = 1.6126 D_i^{\frac{1}{3}} \nu^{\frac{1}{6}} \omega^{-\frac{1}{2}} \tag{A.1}$$

δ_i.......diffusion layer thickness in m
D_i.......diffusion coefficient in m^2 s^{-1}
ν.......kinematic viscosity in m^2 s^{-1}
ω.......rotation rate in s^{-1}

The addition of a buffer complicates the determination of a precise value for the diffusion layer thickness [47,48]. However, previous studies have shown that the effective diffusion layer thickness can still be approximated by the weighted average of the contributions of the two fastest diffusing species H$^+$ and OH$^-$ in the bulk solution [26], as shown in Eq. (A.2).

$$\delta_{\text{eff}} = \frac{c_{\text{H}^+}\delta_{\text{H}^+} + c_{\text{OH}^-}\delta_{\text{OH}^-}}{c_{\text{H}^+} + c_{\text{OH}^-}} \tag{A.2}$$

Appendix B. Experimental

Standard sample preparation methods immobilise nanoparticles by drying a suspension of dispersed nanoparticles on the electrode surface or immersing the electrode in a nanoparticle suspension [49,50]. Because this leads to a rather weak adhesion, nanoparticle-related electrochemical characterisation is therefore limited to stagnant solutions and the use of a rotating disk electrode with a defined diffusion layer thickness would cause the nanoparticles to be washed away. Alternatively, other immobilisation techniques such as a direct synthesis method, self-assembly of nanolithography lead to nanoparticles where the surface area may be hard to be determined. Due to this, simulations have been compared to a flat electrode surface. Results are still in agreement with the presented model even for the limit of a very large particle radius ($r \to \infty$). In simple terms, a flat electrode surface can be approximated by a particle with very large or infinite radius. Cyclic voltammetry (CV) measurements in buffered solutions were collected using a rotating disk electrode (RDE) set to 2500 rpm and a Solartron Modulab PSTAT 1MS/s connected to a unified power system (APC smart-UPS C SMC1500C, Stronghold Services Corporation, London, Canada) and isolated ground power, to minimize electrical noise. A glassy carbon electrode was used as the working electrode, a platinum (Pt) wire as the counter electrode, and a Ag/AgCl/saturated KCl electrode as the reference electrode. For each measurement, the open circuit potential was measured for 1 min, and then, a potential was scanned from 1.5 V to -1.5 V vs. this reference electrode or from -1.5 V to 1.5 V (two separate CV runs for each buffer concentration) at a scan rate of 10 mV s^{-1}. Varying concentrations of 0.5, 1, 5, and 10 mM carbonate buffer in 5 g L^{-1} sodium chloride were prepared using ultrapure water and sodium bicarbonate. The buffered solutions were each adjusted to pH 7.4 using 8 M NaOH and 5 % HCl. The measurements were run under de-aerated conditions, by purging with nitrogen gas at room temperature (22 °C). Prior to, and in between each measurement in buffered solution, the glassy carbon electrode was cleaned by rinsing with ultrapure water, running a full cycle (in the scan direction of the prior measurement) in 1 M HNO$_3$, and rinsing again with ultrapure water.

References

[1] Electrochemistry, C. Hamann, A. Hamnett, W. Vielstich (Eds.), Wiley VCH, Weinheim, 2007.
[2] T. Reier, M. Oezaslan, P. Strasser, Electrocatalytic oxygen evolution reaction (OER) on Ru, Ir, and Pt catalysts: a comparative study of nanoparticles and bulk materials, ACS Catal. 2 (2021) 1765–1772.
[3] B. Zhang, A. Sels, G. Salassa, S. Pollitt, V. Truttmann, C. Rameshan, J. Llorca, W. Olszewski, G. Rupprechter, T. Bürgi, N. Barrabés, Ligand migration from cluster to support: a crucial factor for catalysis by thiolate protected gold clusters, Chem. Cat. Chem. 10 (2018) 5372–5376.
[4] J. Monzó, Y. Malewski, R. Kortlever, F. Vidal-Iglesias, J. Solla-Gullón, M. Koper, P. Rodriguez, Enhanced electrocatalytic activity of Au@Cu core@shell nanoparticles towards CO$_2$ reduction, J. Mater. Chem. A 3 (2015) 23690.
[5] C. Doñate-Buendia, P. Kürnsteiner, F. Stern, M. Wilms, R. Streubel, I. Kusoglu, J. Tenkamp, E. Bruder, N. Pirch, S. Barcikowski, K. Durst, J. Schleifenbaum, F. Walther, B. Gault, B. Gökce, Microstructure formation and mechanical properties of ODS steels built by laser additive manufacturing of nanoparticle coated iron-chromium powders, Acta Mat. 206 (2021) 116566.
[6] X. Chen, H. Yan, Effect of nanoparticle Al$_2$O$_3$ addition on microstructure and mechanical properties of 7075 alloy, Int. J. Metalcasting 28 (2015) 337–344.
[7] K. McNamara, S. Tofail, Nanoparticles in biomedical applications, Adv. Phys. 2 (2017) 54–88.

[8] J. Yan, K. Bao, T. Liu, J. Cao, Minutes periodic wet chemistry engineering to turn bulk Co-Ni foam into hydroxide based nanosheets for efficient water decomposition, Chem. Eng. J. 401 (2020) 126092.

[9] Y. Huang, J. Ren, X. Qu, Nanozymes: classification, catalytic mechanisms, activity regulation, and applications, Chem. Rev. 119 (2019) 4357–4412.

[10] A. Singh, P. Laux, A. Luch, C. Sudrik, S. Wiehr, A. Wild, G. Santomauro, J. Bill, M. Sitti, Review of emerging concepts in nanotoxicology: opportunities and challenges for safer nanomaterial design, Toxicol. Mech. Methods 29 (2019) 378–387.

[11] A. Tiple, V. Badwaik, S. Padwad, R. Chaudhary, N. Singh, A review on nanotoxicology: aquatic environment and biological system, Mater. Today. Proc. 29 (2020) 1246–1250.

[12] G. Oberdörster, T. Kuhlbusch, In vivo effects: methodologies and biokinetics of inhaled nanomaterials, NanoImpact 10 (2018) 38–60.

[13] J. Rennick, A. Johnston, R. Parton, Key principles and methods for studying the endocytosis of biological and nanoparticle therapeutics, Nat. Nanotechnol. 16 (3) (2021) 266–276.

[14] K. Saha, S. Agasti, C. Kim, X. Li, V. Rotello, Gold nanoparticles in chemical and biological sensing, Chem. Rev. 112 (5) (2012) 2739–2779.

[15] L. Yao, J. Daniels, A. Moshnikova, S. Kuznetsov, A. Ahmed, D. Engelman, Y. Reshetnyak, O. Andreev, pHLIP peptide targets nanogold particles to tumors, Proc. Natl. Acad. Sci. 110 (2) (2013) 465–470.

[16] J. Tam, J. Tam, A. Murthy, D. Ingram, L. Ma, K. Travis, K. Johnston, K. Sokolov, Controlled assembly of biodegradable plasmonic nanoclusters for near-infrared imaging and therapeutic applications, ACS Nano 4 (4) (2010) 2178–2184.

[17] E. Dreaden, A. Alkilany, X. Huang, C. Murphy, M. El-Sayed, The golden age: gold nanoparticles for biomedicine, Chem. Soc. Rev. 41 (7) (2012) 2740–2779.

[18] K. Midander, P. Cronholm, H. Karlsson, K. Elihn, L. Möller, C. Leygraf, I. Odnevall-Wallinder, Surface characteristics, copper release, and toxicity of nano- and micrometer-sized copper and copper(II) oxide particles: across-disciplinary study, Small 5 (3) (2009) 389–399.

[19] J. Shi, Y. Hedberg, M. Lundin, I. Odnevall-Wallinder, H. Karlsson, L. Möller, The hemolytic properties of synthetic nano- and porous- silica particles: the effect of surface properties and the protection by the plasma corona, Acta Biomater. 8 (9) (2012) 3478–3490.

[20] A. Nel, L. Mädler, D. Velegol, T. Xia, E. Hoek, P. Somasundaran, F. Klaessig, V. Castranova, M. Thompson, Understanding biophysicochemical interactions at the nanobio interface, Nat. Mater. 8 (7) (2009) 543–557.

[21] S. Rajagopalan, G.-K. Sadeer, R. Brook, Air pollution and cardiovascular disease, J. Am. Coll. Cardiol. 72 (17) (2018) 2054–2070.

[22] U. Carlander, K. Midander, Y. Hedberg, G. Johanson, M. Bottai, H. Karlsson, Macrophage-assisted dissolution of gold nanoparticles, ACS Appl. Bio Mater. 2 (3) (2019) 1006–1016.

[23] S. McCarrick, K. Midander, M. Krausova, U. Carlander, H. Karlsson, Gold nanoparticles dissolve extracellularly in the presence of human macrophages, Int. J. Nanomed. 16 (2021) 5895–5908.

[24] K. Luyts, D. Napierska, B. Nemery, P. Hoet, How physico-chemical characteristics of nanoparticles cause their toxicity: complex and unresolved interrelations, Env. Sci. Process. Impact. 15 (2013) 23–38.

[25] W. Poon, Y.-N. Zhang, B. Ouyang, B. Kingston, J. Wu, S. Wilhelm, W. Chan, Elimination pathways of nanoparticles, ACS Nano 13 (5) (2019) 5785–5798.

[26] M. Auinger, I. Katsounaros, J. Meier, S. Klemm, P. Biedermann, A. Topalov, M. Rohwerder, K. Mayrhofer, Near-surface ion distribution and buffer effects during electrochemical reactions, Phys. Chem. Chem. Phys. 13 (2011) 16384–16394, https://doi.org/10.1039/c1cp21717h.

[27] M. Eigen, Methods for investigation of ionic reactions in aqueous solutions with half-Times as short as 10^{-9} sec - application to neutralization and hydrolysis reactions, Discuss Faraday Soc. 17 (1954) 194–205.

[28] An Elementary Treatise on Fourier's Series, and Spherical, Cylindrical, and Ellipsoidal Harmonics, with Applications to Problems in Mathematical Physics, W. Byerly (Ed.), Dover, New York, 1959.

[29] CRC Handbook of Chemistry and Physics, D. Lide (Ed.), CRC Press, Boca Raton, Florida, Internet Version, 2010. http://www.hcpnetbase.com

[30] R. Zeebe, On the molecular diffusion coefficients of dissolved CO_2; HCO_3^- and CO_3^{2-} and their dependence on isotopic mass, Geochim. Cosmochim. Acta 75 (2011) 2483–2498.

[31] M. Vukmirovic, N. Vasiljevic, N. Dimitrov, K. Sieradzki, Diffusion-limited current density of oxygen reduction on copper, J. Electrochem. Soc. 150 (2003) B10–B15.

[32] A. Oleinick, O. Sliusarenko, I. Svir, C. Amatore, Review - nanostructured electrodes as random arrays of active sites: modeling and theoretical characterization, J. Electrochem. Soc. 167 (2020) 013530.

[33] G. Pireddu, I. Svir, C. Amatore, A. Oleinick, Modelling diffusion at random arrays of electrodes: revisiting the voronoi tessellation concept, Electrochim. Acta 365 (2021) 137338.

[34] Electrochemical Methods: Fundamentals and Applications, A. Bard, L. Faulkner (Eds.), John Wiley and Sons Inc., New York, 2001.

[35] S. Hamel, B. Buckley, P. Lioy, Bioaccessibility of metals in soils for different liquid to solid ratios in synthetic gastric fluid, Env. Sci. Technol. 32 (1998) 358–362.

[36] J. Maltby, S. Pytka, N. Watson, R.M. Cowan, G. Fick, Drinking 300 mL of clear fluid two hours before surgery has no effect on gastric fluid volume and pH in fasting and non-fasting obese patients, Can. J. Anesth. 51 (2004) 111–115.

[37] C. Winterbourn, M. Hampton, J. Livesey, A. Kettle, Modeling the reactions of superoxide and myeloperoxidase in the neutrophil phagosome: implications for microbial killing, J. Biol. Chem. 281 (52) (2006) 39860–39869.

[38] J. Slauch, How does the oxidative burst of macrophages kill bacteria? Still an open question, Mol. Microbiol. 80 (2011) 580–583.

[39] E. Nader, S. Skinner, M. Romana, R. Fort, N. Lemonne, N. Guillot, A. Gauthier, S. Antoine-Jonville, C. Renoux, M.-D. Hardy-Dessources, E. Stauffer, P. Joly, Y. Bertrand, P. Connes, Blood rheology: key parameters, impact on blood flow, role in sickle cell disease and effects of exercise, Front. Physiol. 10 (2019) 1329.

[40] The Cardiovascular System: Blood Vessels, Human anatomy & Physiology, E. Marieb, K. Hoehn (Eds.), Pearson Education, London, 2013.

[41] M. König, J. Vaes, E. Klemm, D. Pant, Solvents and supporting electrolytes in the electrocatalytic reduction of CO_2, iScience 19 (2019) 135–160.

[42] Y. Yi, G. Weinberg, M. Prenzel, M. Greiner, S. Heumann, S. Becker, R. Schlögl, Electrochemical corrosion of a glassy carbon electrode, Catal. Today 295 (2017) 32–40.

[43] J. Kwon, P. Choi, K. Eom, A comparison study on the carbon corrosion reaction under saturated and low relative humidity conditions via transmission line model-Based electrochemical impedance analysis, J. Electrochem. Soc. 168 (2021) 064515.

[44] O. Ivanova, F. Zamborini, Electrochemical size discrimination of gold nanoparticles attached to glass/indium-tin-oxide electrodes by oxidation in bromide–containing electrolyte, Anal. Chem. 82 (2010) 5844–5850.

[45] O. Ivanova, F. Zamborini, Size-dependent electrochemical oxidation of silver nanoparticles, J. Am. Chem. Soc. 132 (2010) 70–72.

[46] W. Plieth, Electrochemical properties of small clusters of metal atoms and their role in the surface enhanced raman scattering, J. Phys. Chem. 86 (1982) 3166–3170.

[47] A. Zelinsky, B. Pirogov, Effective thickness of the diffusion layer during hydrogen ion reduction in aqueous hydrochloric acid solutions, Russ. J. Electrochem. 44 (2008) 585–593.

[48] I. Streeter, R. Compton, Are steady state diffusion layer thicknesses potential independent? Russ. J. Electrochem. 44 (2008) 123–130.

[49] K. Tschulik, C. Batchelor-McAuley, H.-S. Toh, E. Stuarta, R. Compton, Electrochemical studies of silver nanoparticles: a guide for experimentalists and a perspective, Phys. Chem. Chem. Phys. 16 (2014) 616–623.

[50] A. Kumar, Y. Zhang, D. Li, R. Compton, A mini-review: how reliable is the drop casting technique? Electrochem. Commun. 121 (2020) 106867.